J Mater Sci (2017) 52:4587–4598

Micro-mechanism during long-term creep of a precipitation-strengthened Ni-based superalloy

Xiaoqing Song[1], Liying Tang[1,*], Zheng Chen[1], and Rongcan Zhou[2]

[1] State Key Laboratory of Solidification Processing, Northwestern Polytechnical University, Xi'an 710072, Shaanxi, China
[2] National Energy R & D Center of Clean and High-Efficiency Fossil-Fired Power Generation Technology, Xi'an Thermal Power Research Institute Co. Ltd, Xi'an 710032, Shaanxi, China

Received: 29 July 2016
Accepted: 20 December 2016
Published online: 28 December 2016

ABSTRACT

The long-term creep behavior of a Ni-based superalloy Haynes 282 at 700 and 750 °C was investigated. The creep curves exhibit the traditional shape with three creep stages. The coarsening of the γ′ phase during creep at 700 and 750 °C can be detected. The applied stress plays an important role in the coarsening of γ′ particles because of the lattice misfit and the difference of elastic modulus between the matrix and γ′ phase. Dislocation shearing into the γ′ phase and the Orowan process are the dominant creep deformation mechanisms at 700 °C/322 MPa. Dislocations tend to shearing into γ′ phase at first; nevertheless, the Orowan bowing mechanism replaces the process of shear as the coarsening of γ′ phase. The dominant deformation mechanism at 750 °C/187 MPa and 750 °C/215 MPa is dislocation gliding combined with dislocation climbing. Dislocation networks distributed in the interface of γ/γ′ phase may change the direction of dislocations and promote them to climb over the γ′ phase. The fracture surfaces were observed by scanning electron microscopy. Intergranular fracture is the dominant failure mode of the three samples because of the softening of grain boundary and stress concentration. Quasi-cleavage fracture, which are attributed to the stress concentration at the carbides/matrix interface, can be observed on the fracture surface of the specimen crept at 700 °C/322 MPa, whereas dimples with small precipitates inside can be detected on the fracture surface of the samples crept at 750 °C/187 MPa and 750 °C/215 MPa.

Introduction

700 °C advanced ultra-supercritical (A-USC) fossil-fired power plants with a steam pressure of 35–37.9 MPa have been developed for decades to meet the enhanced requirement for higher efficiency and reduced pollutant emissions [1–3]. The superheater and reheater tubes for 700 °C A-USC power plant that operate at 750 °C (50 °C higher than the steam temperature [4]) have to withstand the most extreme surroundings. These conditions exceed the capability of traditional materials, such as austenitic

Address correspondence to E-mail: 13991923616@163.com

DOI 10.1007/s10853-016-0703-0

and ferrite steels, and fall into regimes only suitable for nickel-based superalloys [5, 6]. Haynes 282, an age-hardened Ni-based superalloy, is a promising candidate for 700 °C A-USC power plant applications because of its combination of excellent creep strength, thermal stability, and resistance to high-temperature oxidation in the 649–927 °C range [7–9]. In the age-hardened condition, the microstructure of Haynes 282 consists of spherical γ′ phase coherently embedded in the γ matrix, with a few Mo-rich M_6C carbides and Cr-rich $M_{23}C_6$ carbides distributed intragranularly and at grain boundary (GB). The materials for superheater and reheater components should exhibit superior mechanical properties, especially creep resistance, when working at 750 °C. The creep property of alloy is dominated by microstructural features and deformation mechanisms [10]. Rozman et al. [11] investigated the fatigue behavior of Haynes 282 alloy at 550–750 °C and revealed that transgranular cracks occurred at all temperatures with little intergranular fracture. A corresponding increase in crack growth rates was observed with the increase of test temperature. Unfortunately, there are limited investigations and data available on the creep behaviors of this alloy.

A variety of research on different Ni-based alloys has been presented in recent years. Haan et al. [12] investigated the creep property of 617B superalloy at 725 °C and found that the precipitation of $M_{23}C_6$ carbides, mainly in grain boundaries, starts almost immediately after thermal exposure. The $M_{23}C_6$ carbides reduce the ductility of the alloy, as well as the minimum creep rate. Many Ni-based alloys, including Haynes 282, owe their creep strength to a uniformly dispersed γ′ phase [13–16]. The γ′ particles interacting with dislocations during creep may restrain the slipping of dislocations, decrease the strain rate during steady-state creep stage, and enhance the creep resistance to prolong the lifetime. The motion of the dislocations during creep includes dislocations slipping in the matrix, climbing and shearing of the γ′ precipitate, which leads to the formation of anti-phase boundary (APB) [14, 17]. Furthermore, dislocation networks may form at the interfaces of γ/γ′ particles, which release the misfit stress between the matrix and γ′ phase, alleviate the concentration of stress, prevent the dislocations from shearing into the γ′ particle, and improve the creep property of the alloy [18–20]. Grain boundaries also have significant influence on the creep property. The motion of dislocations becomes easier in grains with increasing temperature; therefore, the strength of GB becomes important to restrain the slipping of dislocations, and insufficient GB strength may speed the failure [4]. The carbides, γ′ particles, and GBs will interact with dislocations during creep, which have a significant influence on the creep property of superalloys.

In the present study, the high-temperature creep behavior of Haynes 282 alloy at 700 and 750 °C was investigated to evaluate its high-temperature creep property. The fracture surfaces were observed by scanning electron microscopy (SEM) to investigate the fracture behavior, and the analyses of microstructural evolutions and dislocation configurations were conducted by transmission electron microscopy (TEM) to investigate the effect of precipitated phases and dislocations on the creep behavior of Haynes 282.

Experimental procedure

The Haynes 282 alloy used for this investigation was provided by Haynes International Inc. in the form of bars in solution-annealed conditions, and the typical solution annealing temperature was in the range of 1121–1149 °C. Table 1 shows the chemical composition of the Haynes 282 alloy. The bars were given a standard two-step age-hardened treatment of 1010 °C/2 h/air-cool + 788 °C/8 h/air-cool before the creep test. The first step of heat treatment results in the precipitation of $M_{23}C_6$ carbides at the GBs, which improve the creep strength. The purpose of the

Table 1 Chemical composition of Haynes 282 alloy (wt%)

Ni	Cr	Mo	Co	Ti	Fe	Al	Mn	Si	C	B	Nb	Cu	W	Other
Bal.	19.65	8.73	10.28	2.13	1.2	1.53	0.06	0.06	0.064	0.004	0.1[a]	0.01[a]	0.01[a]	–

[a] Maximum

second step is to form γ′ particles. The cylindrical creep specimens with a gage length of 100 mm and a gage diameter of 10 mm were machined from the bar in the longitudinal direction.

The uniaxial constant-load creep tests were conducted by creep test machines in air under 700 °C/322 MPa, 750 °C/187 MPa, and 750 °C/215 MPa, respectively. The test temperature was kept constant within ±1 °C for each specimen. 700 and 750 °C were chosen as the test temperatures because 750 and 700 °C are the operating temperatures of superheater/reheater tubes and pipes, respectively. The stress is determined by the predicted creep life of 10,000 and 20,000 h according to Ref. [21]. After the creep test, a ZEISS SUPER-55 type field emission scanning electron microscope (FE-SEM) was used to observe the fracture surface. The cross-section of the fracture was also observed by FEI Quanta-400HV SEM, and backscattered electrons (BSE) were used for the observation. The specimens were mechanically polished and etched in a solution of HCl, H_2SO_4, and $CuSO_4$ before the observation by BSE. A JEM-3010 high-resolution transmission electron microscope (HR-TEM) was used to evaluate dislocation particle interaction. The microstructure of Haynes 282 alloy prior to creep was also detected by TEM. The TEM disks were cut parallel to the stress axis of the creep samples and were manually ground to 40 μm thickness. Next, the foils were perforated by a twin-jet electropolisher in a solution of 10% (volume fraction) perchloric acid and 90% ethanol under the conditions of 15 V and −30 °C. Nano Measurer software was used to measure the average diameter of γ′ phase according to the TEM images. The number of measured γ′ particles is no less than 100 for the stressed zone and gripped end of each samples.

Results

Creep curves

The creep tests of Haynes 282 after age-hardened treatment were conducted under different conditions, and the results are shown in Fig. 1. The lifetime of the specimen crept at 750 °C/215 MPa was 7640 h, which increased to 13,630 h when the creep stress decreased to 187 MPa. At the same time, the alloy crept at 700 °C/322 MPa suffered from fracture after 9117 h. The sample crept at 700 °C/288 MPa is still running. The elongations were 11.1, 16.1, and 15.8% for samples tested at 700 °C/322 MPa, 750 °C/187 MPa, and 750 °C/215 MPa, respectively.

The creep strain rates plotted as a function of time are shown in Fig. 1b. The transient creep at the moment of applying the load is significant. The transient strain is sensitive to the applied stress and becomes smaller with the decrease of stress. The creep curves can be divided into three stages, i.e., primary, secondary, and tertiary. In the primary creep stage, the creep rate decreases rapidly with increasing creep time because dislocations can slip easily in the matrix when applying the load, and the density of dislocations increases sharply as the creep continues, which induces strain hardening to decrease the strain rate. The secondary creep, i.e., the

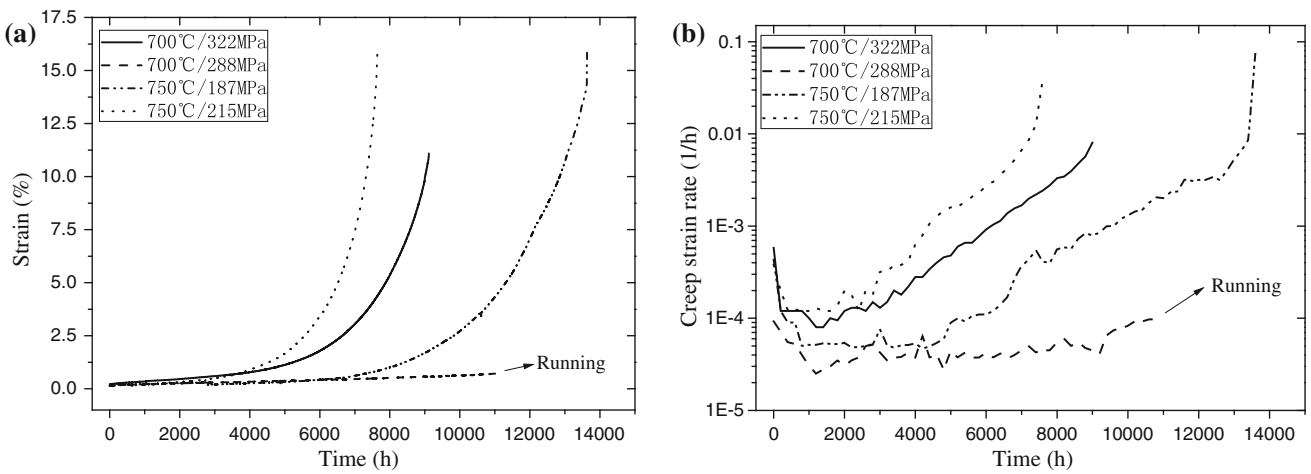

Figure 1 Creep curves of Haynes 282 under various experimental conditions. **a** Creep strain (%) and **b** creep strain rate (1/h) plotted as a function of time (h).

steady-state creep, activates when the creep rate of the primary stage reaches the minimum. The creep rate remains approximately constant during the secondary creep stage. Steady-state creep is induced by the balance between strain hardening and recovery softening [22]. Haynes 282 alloy does not have such an extended steady-state creep regime as simple metals [23]. The steady-state creep rates of the alloys crept at 700 °C/322 MPa, 750 °C/187 MPa, and 750 °C/215 MPa were 1.09×10^{-4}, 4.91×10^{-5}, and 1.17×10^{-4}%/h, respectively, and the rates of tertiary creep increase sharply until rupture.

The steady-state creep rate ($\dot{\varepsilon}_{ss}$) of superalloy crept at high temperature can be expressed using the Dorn law as follows [20]:

$$\dot{\varepsilon}_{ss} = A\sigma_a^n \exp(-Q_C/RT), \quad (1)$$

where A is a constant, σ_a is the applied stress, n and Q_C are the apparent stress exponent and activation energy, respectively, and R is the gas constant. Equation (1) can be simplified to Eq. (2) [20] when the temperature is considered constant:

$$\lg \dot{\varepsilon}_{ss} - n \lg \sigma_a = \text{const}. \quad (2)$$

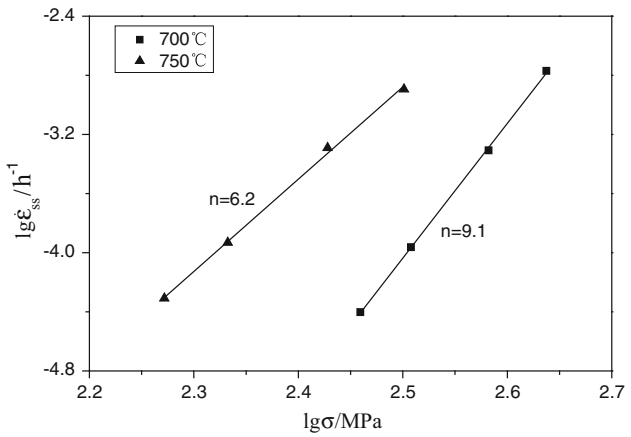

Figure 2 Applied stress dependence of the strain rate during steady-state creep of Haynes 282 at 700 and 750 °C (some points are obtained from additional experiments, which are not discussed in this paper).

According to Eq. (2), the apparent stress exponent of Haynes 282 during steady-state creep is 9.1 and 6.2 for 700 and 750 °C, respectively (Fig. 2), which is consistent with the investigation of Boehlert et al. [24]. The difference of the n value indicates a possible change in creep deformation mechanisms.

Deformation microstructures

The diameter of γ′ particles is 25 nm before creep test. The coarsening of γ′ particles during creep at 700 and 750 °C can be observed, and the diameters of the γ′ precipitates, which increase with increased temperature and creep time, are listed in Table 2. The diameter of γ′ particles in the stressed zone is larger than that in the gripped end in the sample crept at 700 °C. The result is consistent with the conclusion of Santella et al. [25], where the misfit between the matrix and γ′ phase is 0.025% at 700 °C and −0.025% at 750 °C of the Haynes 282 alloy. The elastic modulus of γ′ phase is considerably larger than the matrix in Haynes 282 alloys, so it can be speculated that γ′ particles present less deformation during creep. It was defined as "positive modulus system" [26]. The matrix/γ′ phase interface is coherent for Haynes 282 alloy, and therefore the effect of elastic strain energy is larger than the interfacial energy on the coarsening of γ′ phase. Because of the applied tensile stress, the lattice constant of the matrix in stressed zone increases, while the lattice constant of γ′ remains constant during creep at 700 °C. It induces the decrease of elastic strain energy. Therefore, the coarsening of γ′ phase, which distributes in stressed zone, is promoted. As can be observed in Table 2, the diameter of γ′ particles in the stressed zone is slightly smaller than that in the gripped end in the samples crept at 750 °C. However, the scatter is slightly large, and further investigation is necessary to decide the effect of stress on the coarsening of γ′ phase at 750 °C. Because the misfit between the matrix/γ′ is fairly small, the process of γ′ particle coarsening is not extremely sensitive to the applied stress. The

Table 2 Diameter of γ′ particles after creep rupture of Haynes 282 alloy (nm)

	700 °C/322 MPa	Standard deviation	750 °C/187 MPa	Standard deviation	750 °C/215 MPa	Standard deviation
Stressed zone	74.2	4.2	142.8	5.1	112.3	5.5
Gripped end	61.8	3.6	152.8	5.5	123.5	4.9

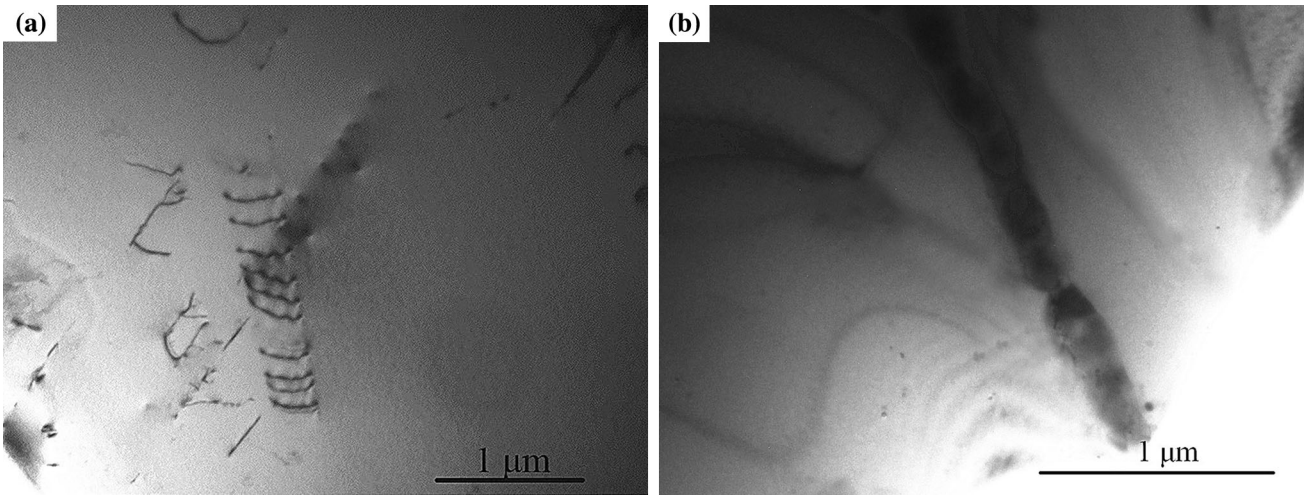

Figure 3 TEM images showing the microstructures of the alloy prior to creep deformation.

difference of the γ′ particle diameters between the stressed zone and the gripped end is 10.0–12.4 nm. Nevertheless, the shape of γ′ particles of this alloy remains spherical during the long-term creep, as illustrated in Fig. 4.

The microstructures of Haynes 282 alloy prior to creep deformation are illustrated in Fig. 3. A few dislocations can be detected within the grains, while few dislocations pile up at GBs. Figure 4 shows the TEM images of the alloy after creep rupture under different conditions. As compared with Fig. 3, the density of dislocations increases sharply during creep deformation. Sinuous dislocations are observed in the sample crept at 700 °C/322 MPa, which indicates dislocation slip (marked by arrow B in Fig. 4a) [4]. Dislocations cut through the γ′ phase with APB (arrow C) are present in Fig. 4b. Yu et al. [27] detected the pairs of APB-coupled dislocations in specimens of SRR99 alloy after creep rupture at 700 °C. According to [27, 28], the formation of APBs results from the a/2 ⟨110⟩ dislocations cutting into the γ′ phase, as well as the pairs of APB-coupled dislocations. Significant amounts of dislocation loops distributed within the grains are marked by arrow A in Fig. 4a. There are threshold stresses for the creep of the superalloy [22], and the threshold stress of dislocation shearing into the γ′ particle is lower than that of the Orowan process, indicating that dislocations tend to shear into the γ′ phase rather than bypass through the Orowan bowing mechanism. However, the threshold stress of dislocation shearing into the γ′ particle remains constant during creep, while the threshold stress of the Orowan process decreases with the γ′ particle coarsening. Therefore, the Orowan bowing mechanism replaces the process of dislocation shearing into the γ′ particles when the γ′ particles are large enough. The diameter of γ′ particles plays an important role in the process of dislocation shearing into γ′ phase [4, 29]. Dislocation slip in the matrix can also be observed obviously in the samples crept at 750 °C/187 MPa and 750 °C/215 MPa. The microstructure of the alloy after creep rupture at 750 °C/187 MPa and 750 °C/215 MPa is shown in Fig. 4c, d and e, f, respectively. The dislocations pile up at the interfaces of the γ/γ′ phase (arrow D) to form the dislocation networks in the sample crept at 750 °C/187 MPa (Fig. 4c, d), as well as the sample crept at 750 °C/215 MPa (arrow F in Fig. 4e, f). Dislocations climbing over the γ′ particles (arrow E and G) can also be detected (Fig. 4d, e). Few dislocations cut through the γ′ phase with APBs and dislocation loops are discovered in the specimens crept at both 750 °C/187 MPa and 750 °C/215 MPa.

As illustrated in Fig. 5a, dense dislocations pile up at the GB carbides in sample after creep rupture at 700 °C/322 MPa. Compared with Fig. 3b, the coarsening of the GB carbides can be detected obviously. GB carbides improve the high-temperature strength of GBs and restrain the motion of dislocations effectively during creep of Haynes 282 alloy. Moreover, carbides and μ phases, which precipitate during the long-term creep and distribute within the grains, can also hinder the motion of dislocations, as illustrated in Fig. 5b, c. Topological close-packed μ phase is an A_7B_6-type intermetallic compound with rhombohedral structure

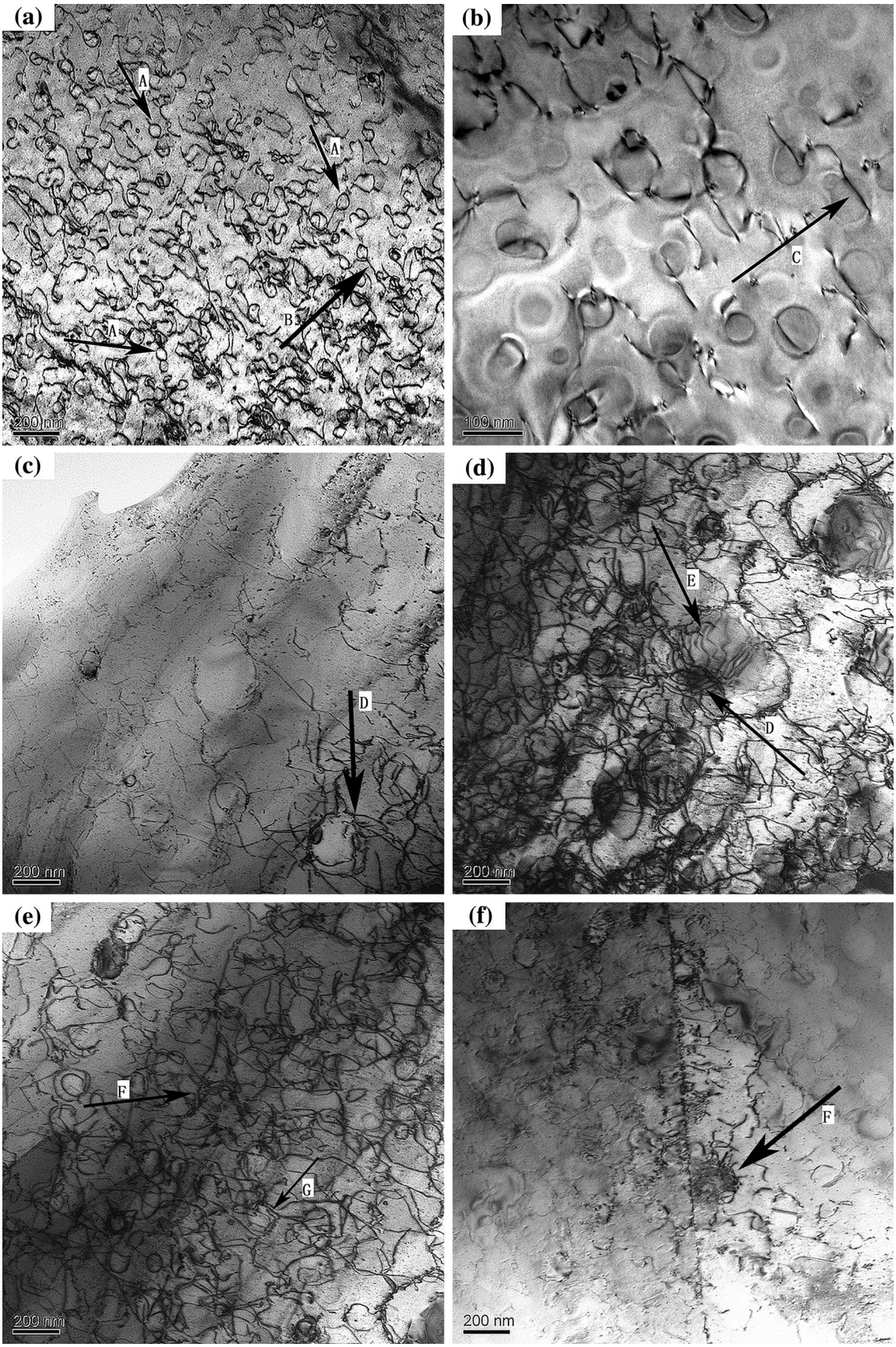
(a)
A
A
A
B
200 nm
(b)
C
100 nm
(c)
D
200 nm
(d)
E
D
200 nm
(e)
F
G
200 nm
(f)
F
200 nm

◀**Figure 4** TEM images of the alloy after creep rupture under different conditions. **a** and **b** Dislocation loops (*arrow A*), dislocation glide (*arrow B*), and the APBs (*arrow C*), which are formed by dislocation shearing into the γ′ phase, in the specimen crept at 700 °C/322 MPa. **c** Dislocations piled up at the interface of γ/γ′ particles (*arrow D*) in the sample crept at 750 °C/187 MPa and **d** dislocations climbing over the γ′ phase (*arrow E*) in the sample crept at 750 °C/187 MPa. **e** and **f** Dislocation networks distributed at the interfaces of the γ/γ′ phase (*arrow F*) and the dislocation climb (*arrow G*) in the sample crept at 750 °C/215 MPa.

(A is occupied by Fe, Co, etc., B is occupied by W, Mo, etc.) [30].

According to Ref. [31, 32], numerous $M_{23}C_6$ carbides precipitate at the GBs and a few M_6C carbides precipitate within the grains during the standard age-hardened treatment of Haynes 282 alloy. During creep deformation, the coarsening of $M_{23}C_6$ carbides can be detected, while more $M_{23}C_6$ and a few M_6C carbides separate out at the GBs. The precipitation and coarsening of M_6C carbides within the grains also can be observed during creep.

Creep fracture

The fracture surfaces of samples after creep rupture under different conditions were examined by SEM, as shown in Fig. 6. All three specimens remain basically round shaped, whereas obvious reduction of the area can be observed. It is indicated that the reduction of area after creep rupture is 17, 33, and 32% at 700 °C/322 MPa, 750 °C/187 MPa, and 750 °C/215 MPa, respectively. It can be observed from Fig. 6 that intergranular fracture is the dominant failure mode of this alloy during creep at 700 °C/322 MPa, 750 °C/187 MPa, and 750 °C/215 MPa. Some quasi-cleavage characters (marked by the arrow in Fig. 6a) are detected simultaneously on the fracture surface of the specimen crept at 750 °C/322 MPa, such as river pattern and tear ridge, is detected simultaneously on the fracture surface of the specimen crept at 700 °C/322MP. Instead of quasi-cleavage fracture, large amounts of small dimples are observed on the GBs on the fracture surface of the samples crept at 750 °C/187 MPa and 750 °C/215 MPa. Small particles inside can be discovered simultaneously (Fig. 6c, e). The fracture surface images of the three samples show secondary cracks.

There are two mechanisms of intergranular rupture behavior [22]. First, flaws, i.e., microcracks, which are observed in the triple junctions, are generated as a consequence of stress concentration, which results from boundary sliding during creep, in the triple junctions (Fig. 7). Second, cavities, which coalesce with each other to form the flaws, originate from precipitates (Fig. 8) and steps at GBs. A high density of secondary cracks and cavities can be observed beneath the fracture surface, with a majority along the GBs (Fig. 7). The secondary cracks have an angle of 45°–90° to the stress axis. GBs perpendicular to the deformation direction are more sensitive to the nucleation of cavities [33]. GBs affect the creep deformation mechanism. In the investigation of Haynes 282 alloy conducted by Boehlert et al. [24], precipitate migration to the GBs, which is aided by diffusion and is beneficial to intergranular cracking, during high-temperature creep is observed as an aspect of the deformation behavior.

Discussion

Song et al. [32] compared the creep property of Haynes 282 alloy with some others and concluded that Haynes 282 alloy has superior creep property to Nimonic 263 and Inconel 740 at 700 and 750 °C. During the tertiary creep stage, a high density of flaws and cavities form both beneath the fracture surface (marked by arrow in Fig. 7a) and at the edge (marked by arrow in Fig. 7c) of the creep samples. It is the main reason for the increasing creep rate during the tertiary creep stage. According to Ref. [34], cavities result from the slip bands, which interact at the GBs, within different grains. Ai et al. [35] investigated the creep fracture mechanism of three single-crystal Ni-based superalloys and demonstrated that cavities can form because of carbide cracking. Additionally, cavities also nucleate at the interface of matrix/carbides, as illustrated in Fig. 8. Liu [31] investigated the creep strength of Haynes 282 alloy at 700 °C and observed that cavities nucleate at the interface of matrix/carbides. GBs and carbides play an important role in the formation of cavities and cracks. During creep, GBs deform through slip and kink, which induce stress concentrations in the connections of the GBs. Thus, microcracks and cavities tend to form [36]. As illustrated in Fig. 8, significant amounts of carbides precipitate in the GBs. The carbides precipitated in the GBs will increase the resistance of crack propagation along the GBs and impede

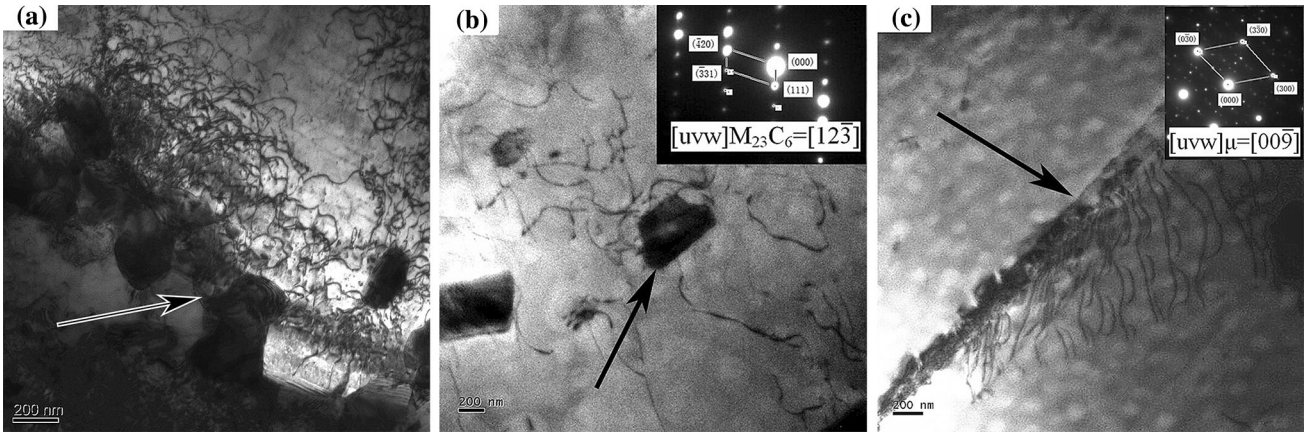

Figure 5 TEM micrographs showing the microstructures of the alloy after creep rupture. **a** Dislocation pile-up near the GBs of the alloy when crept at 700 °C/322 MPa. *Arrows* in the images indicate the GBs.**b** Dislocation tangles at the interface of carbides, which precipitated transgranularly. The diffraction spot of this carbide is shown in the *top right* corner. **c** Dislocation tangles near the interface of the γ/μ phase. The diffraction spot of μ phase is shown in the *top right* corner.

the growth and coalescence of cavities. As the creep continues, creep fracture occurs when the measurement of cracks reaches a critical fraction [22].

The dislocation networks can increase the strength of the alloy by interacting with dislocation slipping in the matrix and by affecting the strength of the γ/γ′ interfaces [37]. Dislocation networks are detected at the γ/γ′ interfaces in samples after creep rupture at 750 °C (Fig. 4c, f). And few dislocation shearing into the γ′ phase can be observed, which can be explained by the effect of dislocation networks. Xie et al. [38] considered that dislocations of different characteristics encounter each other to form dislocation networks at the γ/γ′ interface, which can release the misfit stress of the γ/γ′ phase and stabilize the microstructure of the alloy. During creep, dislocations in the matrix move to the dislocation networks and interact with each other. The reaction between the activated dislocations and the dislocation networks may change their motor directions and promote them to climb over the γ′ particles, which alleviates stress concentration and delays the dislocation shearing into the γ′ particles. However, if the applied stress is large enough, the stress concentration cannot be alleviated completely and also it increases. The dislocation networks may be locally damaged when the value of stress concentration is large enough to cut through the γ′ phase. Once the dislocation networks are damaged, the dislocations may shear into the γ′ phase with the formation of APBs.

Significant amounts of dislocation shearing into the γ′ phase and dislocation loops can be observed in the specimen crept at 700 °C/322 MPa (Fig. 4a, b), whereas dislocation networks cannot be detected at the interface of the γ/γ′ phase, indicating that the dislocation networks have been damaged due to stress concentration. The dislocation loops result from the Orowan bowing mechanism as a consequence of γ′ coarsening. During creep deformation at 750 °C/215 MPa and 750 °C/187 MPa, dislocation networks can be precisely observed at the interfaces of the γ/γ′ phase, and few dislocation loops and dislocation shearing into γ′ phase are observed in the samples, indicating that the value of stress concentration has not exceeded the threshold stress of dislocation shearing into the γ′ phase. According to the analysis above and the apparent stress exponent obtained from Eq. (2), dislocation shearing into the γ′ particles and the Orowan process are the dominant creep deformation mechanisms at 700 °C/322 MPa, and dislocation glide combined with dislocation climb is the dominant deformation mechanism at 750 °C/215 MPa and 750 °C/187 MPa. It is consistent with the conclusion of Guo [22]. Guo [22] investigated the creep behavior of DZ417G at 870 °C and considered that the creep deformation mechanisms of DZ417G are different under high and low stresses. The dislocations bypass the γ′ particles through dislocation climb when the applied stress is smaller than 218 MPa, while the dislocations will shear into the γ′ particles or bypass the γ′ particles

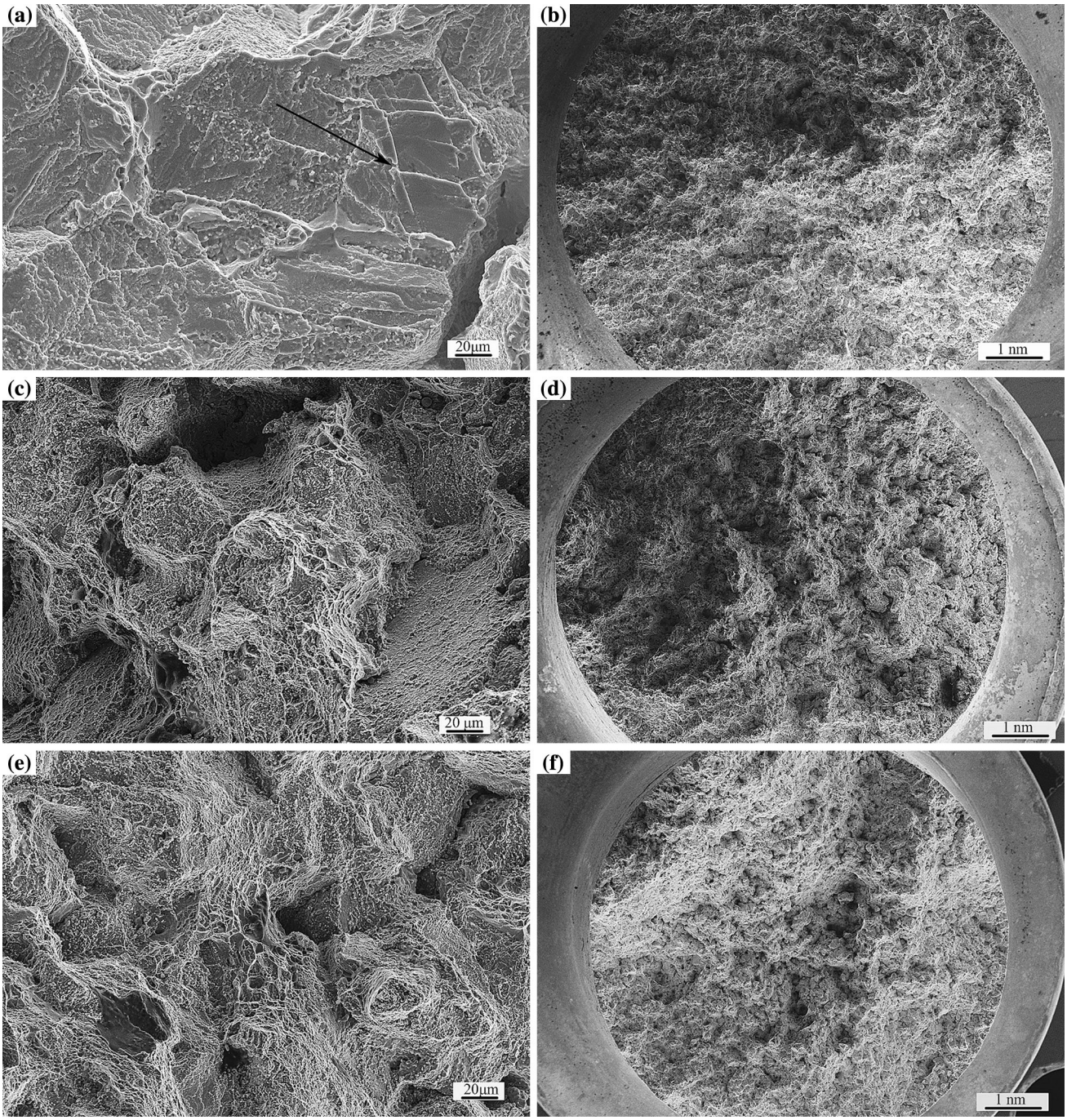

Figure 6 SEM images of the fracture surface of samples crept at **a**, **b** 700 °C/322 MPa, **c**, **d** 750 °C/187 MPa, and **e**, **f** 750 °C/215 MPa.

through the Orowan process when the applied stress is larger than 218 MPa.

During creep at 700 °C/322 MPa of the Haynes 282 alloy, dislocation networks distributed at the interface of the γ'/matrix are damaged. Significant amounts of dislocations pile up at the GBs (as shown in Fig. 5a), which induce stress concentration. The fracture mode is intergranular when the stress concentration is beyond the strength of GBs. Quasi-cleavage fracture is observed on the fracture surface of the sample crept at 700 °C/322 MPa only. Lapin et al. [34] attributed the quasi-cleavage to the coalescence of voids within the adjacent slip bands and the decohesion along the GBs. Nevertheless, Sherry et al. [39] considered the quasi-cleavage to be explained by the decrease of mobile dislocations,

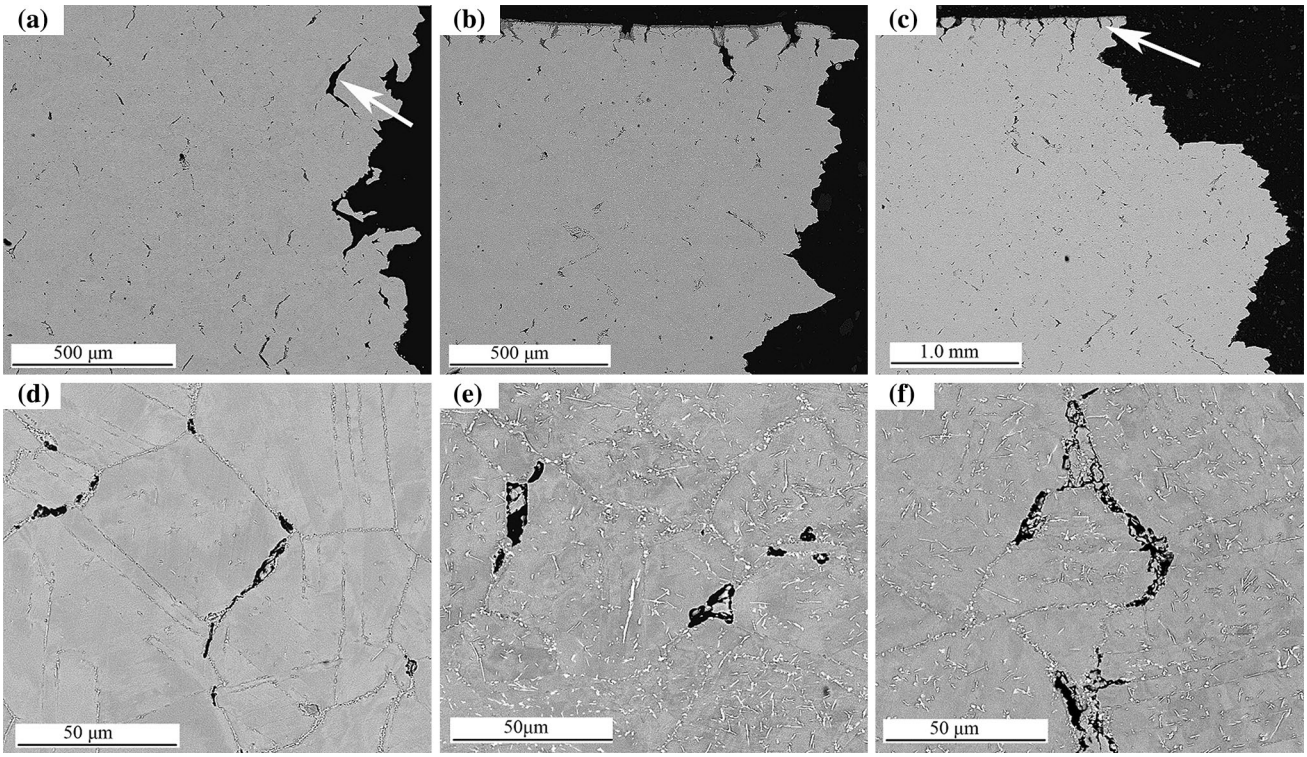

Figure 7 Low-resolution SEM images of the cross-section of the fracture after creep at **a** 700 °C/322 MPa, **b** 750 °C/187 MPa, and **c** 750 °C/215 MPa, respectively. High-resolution SEM images of the cross-section of the fracture after creep at **d** 700 °C/322 MPa, **e** 750 °C/187 MPa, and **f** 750 °C/215 MPa, respectively.

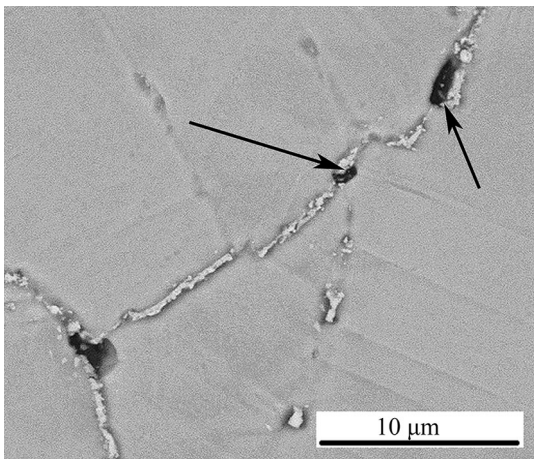

Figure 8 SEM image of the cavity that originates from carbides at the GBs of the sample creep rupture at 750 °C/215 MPa (*arrow* indicates the carbide precipitated in the GB).

which are a consequence of the dislocation pinning mechanism. Dislocations pile up at the carbides/matrix interface and produce stress concentration (Fig. 5b), which can be relieved by cracking of carbides or decohesion of interfaces [23]. Then, transgranular fracture occurs.

In samples crept at 750 °C/187 MPa and 750 °C/215 MPa, significant amounts of dislocations interact with each other to form dislocation networks at the interface of the γ′/matrix. Nevertheless, the GBs are softened at 750 °C. Intergranular fracture is still the dominant failure mode in this alloy during creep at 750 °C/187 MPa and 750 °C/215 MPa (Fig. 6c, e). Large amounts of $M_{23}C_6$ carbides precipitate along the GBs (Fig. 8) during age-hardened treatment, which pile up at the GBs during creep rupture. Therefore, small dimples with carbides inside can be observed on the fracture surface of samples crept at 700 °C/187 MPa and 750 °C/215 MPa.

Conclusions

Creep tests of Haynes 282 were conducted under 700 °C/322 MPa, 750 °C/187 MPa, and 750 °C/215 MPa. Based on the above analysis, the following conclusions can be made:

1. Haynes 282 alloy exhibits excellent creep property at 700 and 750 °C. The lifetimes of specimens crept at 700 °C/322 MPa, 750 °C/187 MPa, and 750 °C/215 MPa are 9117, 13,630, and 7640 h, and the elongations of the ruptured specimens are 11.1, 16.1, and 15.8%, respectively.
2. The coarsening of γ' precipitates during creep at 700 and 750 °C can be detected in Haynes 282 alloy. The applied stress plays an important role in the coarsening of γ' particles because of the lattice misfit and the difference of elastic modulus between the matrix and γ' phase.
3. Dislocation shearing into the γ' phase and the Orowan process are the dominant creep deformation mechanisms at 700 °C/322 MPa. During creep at 700 °C/322 MPa, dislocations tend to shear into γ' phase at first; nevertheless, the Orowan bowing mechanism replaces the process of shear as the coarsening of γ' phase. Intergranular fracture, as well as some quasi-cleavage characters which are attributed to the stress concentration at the carbides/matrix interface, can be detected on the fracture surface of the specimen crept at 700 °C/322 MPa.
4. The dominant deformation mechanism of the samples crept at 750 °C/187 MPa and 750 °C/215 MPa is dislocation gliding combined with dislocation climbing. Dislocation networks distributed in the interface of γ/γ' phase may change the direction of dislocations and promote them to climb over the γ' phase. Intergranular fracture is observed on the two samples because of the softening of GBs and stress concentration, and small dimples with carbides inside can be detected on the fracture surface of the two samples.

Acknowledgement

This work is financially supported by the National Natural Science Foundation of China (Grant Nos. U1361201, 51474176).

Compliance with ethical standards

Conflict of interest The authors declare that they have no conflict of interest.

References

[1] Zhong ZH, Gu YF, Yuan Y, Shi Z (2013) A new wrought Ni–Fe-base superalloy for advanced ultra-supercritical power plant applications beyond 700°C. Mater Lett 109:38–41

[2] Patel SJ, DeBarbadillo JJ, Baker BA, Gollihue RD (2013) Nickel base superalloys for next generation coal fired A-USC power plants. Proced Eng 55:246–252

[3] Chi CY, Yu HY, Xie XS (2013) Critical high temperature materials for 700°C A-USC power plant. World Iron Steel 2:42–59

[4] Yuan Y, Zhong ZH, Yu ZS, Yin HF et al (2015) Tensile and creep deformation of a newly developed Ni-Fe-based superalloy for 700 °C advanced ultra-supercritical boiler applications. Met Mater Int 21:659–665

[5] Manabu T, Ryuichi K (2010) The effect of heat treatments on the creep-rupture properties of a wrought Ni-Cr heat-resistent alloy at 973 K. J Mater Sci 45:4029–4035. doi:10.1007/s10853-010-4481-9

[6] Cabibbo M, Gariboldi E, Spigarelli S, Ripamonti D (2008) Creep behavior of INCOLOY alloy 617. J Mater Sci 43:2912–2921. doi:10.1007/s10853-007-1803-7

[7] Pike LM (2008) Development of a fabricable gamma-prime (γ') strengthened superalloy. TMS, Warrendale, pp 191–200

[8] Brommesson R, Ekh M (2012) Experiments and modelling of the cyclic behaviour of Haynes 282. Tech Mech 32:130–145

[9] Matysiak H, Zagorska M, Andersson J, Balkowiec A et al (2013) Microstructure of Haynes® 282® superalloy after vacuum induction melting and investment casting of thin-walled components. Materials 6:5016–5037

[10] Jo CY, Jones N, Choe SJ, Knowles D (1998) High temperature mechanical properties and creep crack initiation of DS CM186LC for nozzle guide vane. Met Mater 4:1017–1025

[11] Rozman KA, Kruzic JJ, Hawk JA (2015) Fatigue crack growth behavior of nickel-base superalloy Haynes 282 at 550–750 °C. J Mater Eng Perform 24:2841–2846

[12] Haan J, Bezold A, Broeckmann C (2015) Interaction between particle precipitation and creep behavior in the Ni-base alloy 617B: microstructural observations and constitutive material model. Mater Sci Eng A 640:305–313

[13] Sajjadi SA, Nategh A (2001) A high temperature deformation mechanism map for the high performance Ni-base superalloy GTD-111. Mater Sci Eng A 307:158–164

[14] Xie J, Tian S, Shang LJ, Zhou X (2014) Creep behaviors and role of dislocation network in a powder metallurgy Ni-based superalloy during medium-temperature. Mater Sci Eng A 606:304–312

[15] Kvapilova M, Kucharova K, Sklenicka V, Svoboda M et al (2011) Creep behaviour and microstructure changes of model cast Ni-Cr-W-C alloys. Proced Eng 10:839–844

[16] Xie J, Tian S, Zhou X (2013) Creep properties and deformation mechanisms of a FGH95 Ni-based superalloy. J Mater Eng Perform 22:2048–2055

[17] Unocic RR, Viswanathan GB, Sarosi PM, Karthikeyan S et al (2008) Mechanisms of creep deformation in polycrystalline Ni-base disk superalloys. Mater Sci Eng A 483–484:25–32

[18] Viswanathan GB, Sarosi PM, Henry HM, Whitis DD et al (2005) Investigation of creep deformation mechanisms at intermediate temperatures in René 88 DT. Acta Mater 53:3041–3057

[19] Kovarik L, Unocic RR, Li J, Sarosi P et al (2009) Microtwinning and other shearing mechanisms at intermediate temperatures in Ni-based superalloys. Prog Mater Sci 54:839–873

[20] Karthikeyan S, Unocic RR, Sarosi PM, Viswanathan GB et al (2006) Modeling microtwinning during creep in Ni-based superalloys. Scr Mater 54:1157–1162

[21] Tortorelli PF, Yamamoto Y, Maziase PJ, Moser JL et al (2012) Materials for advanced ultra-supercritical (A-USC) steam boilers. In: 26th Annual conference on fossil energy materials, Pittsburgh, PA

[22] Guo JT (2007) Materials science and engineering for superalloys. Science Press Ltd, Beijing

[23] Rettberg LH, Pollock TM (2014) Localized recrystallization during creep in nickel-based superalloys GTD444 and Rene N5. Acta Mater 73:287–297

[24] Boehlert CJ, Longanbach SC (2011) A comparison of the microstructure and creep behavior of cold rolled HAYNES® 230 alloy™ and HAYNES® 282 alloy™. Mater Sci Eng A 528:4888–4898

[25] Santella M, Shingledecker J, Swindeman B (2010) Materials for advanced ultra-supercritical steam boilers. In: 24th Annual conference on fossil energy materials, Pittsburgh, PA

[26] Lu YL, Chen Z, Li YS, Wang YX (2006) Atomic-scale computer simulation for the coarsening mechanism of the cubic alloy including coherent strain energy. Real Met Mater Eng 35:1686–1690

[27] Yu JJ, Sun XF, Jin T, Zhao N et al (2010) High temperature creep and low cycle fatigue of a nickel-base superalloy. Mater Sci Eng A 527:2379–2389

[28] Vorontsov VA, Shen C, Wang Y, Dye D et al (2010) Shearing of γ' precipitates by a $\langle 112 \rangle$ dislocation ribbons in Ni-base superalloys: a phase field approach. Acta Mater 58:4110–4119

[29] Phillipsa PJ, Mills MJ (2013) Fine-scale structure of dislocations and debris in deformed Ni-based superalloy R104. Philos Mag 93:82–95

[30] Tan LM, Zhang YW, Jia J, Han SB (2016) Precipitation of μ phase in nickel-based powder metallurgy superalloy FGH97. J Iron Steel Res Int 23:851–856

[31] Liu YQ (2015) Study on microstructures and properties of Haynes 282 superalloy. Kunming University of Science and Technology, Kunming

[32] Song XQ, Tang LY, Chen Z (2016) Characteristic and application of a new Ni-based superalloy Haynes 282. Mater Rev 30:116–120

[33] Hong HU, Rho BS, Nam SW (2001) Correlation of the $M_{23}C_6$ precipitation morphology with grain boundary characteristics in austenitic stainless steel. Mater Sci Eng A 318:285–292

[34] Lapin J (1999) High temperature creep of precipitation-strengthened Ni_3Al-based alloy. Intermetallics 7:599–609

[35] Ai SH, Lupinc V, Maldini M (1992) Creep fracture mechanisms in single crystal superalloys. Scr Metall Mater 26:579–584

[36] Chen YQ, Pan SP, Liu WH, Cai ZH et al (2015) Effect of precipitates on creep behaviors of Al-Cu-Mg alloy. Chin J Nonferr Metals 25:900–909

[37] Gabb TP, Draper SL, Hull DR, Mackay RA et al (1989) The role of interfacial dislocation networks in high-temperature creep of superalloys. Mater Sci Eng A 118:59–69

[38] Xie J, Tian S, Shang LJ, Zhou X (2014) Creep behaviors and role of dislocation network in a powder metallurgy Ni-based superalloy during medium-temperature. Mater Sci Eng A 606:304–312

[39] Sherry AH, Pilkington R (1993) The creep fracture of a single-crystal superalloy. Mater Sci Eng A 172:51–61